

# Retrieval of Ocean Surface Radial Velocities With RADARSAT-2 Along-Track Interferometry

Mamoon Rashid , *Member, IEEE*, and Christoph H. Gierull , *Senior Member, IEEE*

**Abstract**—This article provides a detailed presentation of the dual-aperture synthetic aperture radar (SAR) data processing scheme for the retrieval of ocean surface radial velocities. This scheme includes processing of raw SAR data, coregistration of along-track interferometric samples, magnitude and absolute phase calibration, and coherent averaging (multilooking). Several approaches for the absolute phase calibration are provided and compared. Some of the attempted approaches can potentially be used over open ocean (i.e., in scenes that do not contain any land). Main goal of attempting different approaches for the absolute phase calibration was to determine their relative performance, and determine the potential feasibility of some approaches over open ocean. The data processing scheme is applied to a RADARSAT-2 dual-channel MODEX-1 acquisition over a section of the Florida Current. For the dataset used in this study, different absolute phase calibration methods yielded similar radial velocity estimates, with relative mean and RMS differences within approximately 0.1 m/s. Estimates from SAR ATI were also compared to estimates from NASA's OSCAR dataset. Comparison of visually identified currents showed close spatial overlap between estimates from the two sources. The RMS difference was found to be approximately 0.30 m/s. This difference can be attributed to the physical and temporal differences between the estimates.

**Index Terms**—Along-track interferometry (ATI), calibration, detection, estimation, radial velocity, surface currents, synthetic aperture radar (SAR).

## I. INTRODUCTION

OCEAN currents can be used by vessels for navigation and routing (e.g., to save travel time and fuel). Ocean currents also play a significant role in determining weather and climate. For example, the Gulf Stream (GS) shapes the climate on four continents. Climate-related changes, such as melting ice, can significantly affect the flow of such currents. In particular, the melting ice from Greenland can potentially alter the flow of the GS current, which can have significant impact on both sides of the Atlantic. Frequent monitoring of such currents is, therefore, essential when studying climate change and its impact on resources and environmental security [1]. Space-based SAR can be used to fill gaps and provide validation for existing data streams.

First reported experiments to measure surface currents with multichannel airborne SAR for along-track interferometry (ATI)

Manuscript received April 30, 2021; revised June 28, 2021 and July 27, 2021; accepted August 20, 2021. Date of publication September 15, 2021; date of current version October 6, 2021. (Corresponding author: Mamoon Rashid.)

The authors are with the Department of National Defence, Defence Research and Development Canada—Ottawa, Ottawa, ON K1A 0Z4, Canada (e-mail: mamoon.rashid@drdc-rddc.gc.ca; christoph.gierull@drdc-rddc.gc.ca).

Digital Object Identifier 10.1109/JSTARS.2021.3110198

were performed by the L-band AirSAR system from NASA Jet Propulsion Laboratory [2]. In SAR ATI, measurements from multiple antenna phase centers, which are separated in the platform along-track direction, are used to compute the interferometric phase that can be converted into platform line-of-sight (LOS) velocity vector—referred as radial velocity—using the imaging geometry. The 1989 Loch Linnhe experiment conducted by the AirSAR system involved concurrent acquisition of ATI data with *in situ* measurements of surface currents, surface wave field, and meteorological conditions [2]. Significant discrepancy was reported between velocity estimates obtained from ATI and *in situ* data. This experiment showed that ATI measurements are not exclusively determined by surface currents, but they also include contributions from wind-dependent surface wave motions. The Loch Linnhe experiment and further work in [3] showed that these contributions are dependent on the wind speed and direction, and radar parameters such as wavelength, polarization, and incidence angle.

First experiment to measure sea surface currents using space-based SAR ATI was performed using the space shuttle [4]. This experiment used SAR ATI to derive surface current velocities in the LOS direction over an area of the Dutch Wadden Sea, and then, compared these SAR measurements to a numerical model that was derived using dominant physical processes. The numerical model was especially developed to describe and predict the consequences of management measures in the Wadden Sea. Experiments to measure river currents or sea surface currents in the vicinity of stationary land using TerraSAR-X/TanDEM-X ATI were conducted by Romeiser *et al.* [5]–[9]. All experiments with the space shuttle and TerraSAR-X/TanDEM-X were performed with X-band SAR. More recently, preliminary results in C-band SAR over the GS using RADARSAT-2 dual-channel ATI have been presented in [10].

Efforts have also been made to study the feasibility of single-channel space-based SAR data for the retrieval of sea surface currents using the Doppler anomaly (DA) method [11]–[14]. Compared to ATI, the DA method requires less volume of data, however, this method does not provide the same high resolution as ATI. Furthermore, the accuracy of surface current radial velocity estimates with DA is limited due to the limitations of satellite steering controls and the limited accuracy of satellite attitude data [15]. Another approach for retrieval of surface currents that has recently gained attention is based on subaperture processing of SAR data acquired with modes that provide sufficiently long exposure time (e.g., spotlight) [16], [17]. However, SAR modes with long exposure times typically have very limited swath

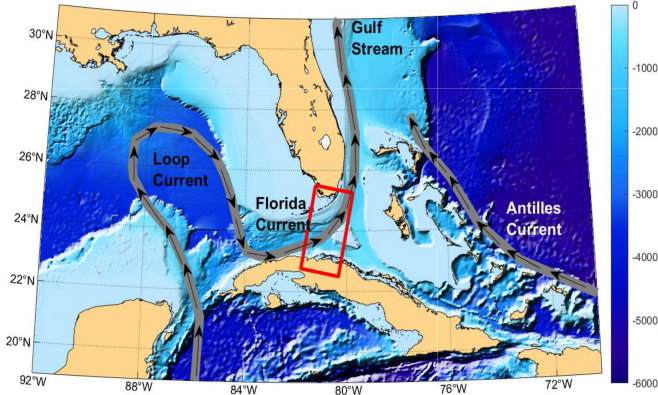


Fig. 1. Schematic diagram of currents (gray) in the vicinity of study area, plotted over bathymetry in meters. The exact test area in this study is denoted by the red rectangle. Warm water current enters the Gulf of Mexico from in between Mexico's Yucatan Peninsula and Cuba forming the Loop Current. This current forms the FC as it moves through Florida Strait. Merger of the Florida and Antilles current forms the GS.

widths, and therefore, may not be suitable for applications that demand large area coverage.

This article extends the work that has been presented in [10] with space-based C-band SAR. It provides a comprehensive data processing scheme for the retrieval of ocean surface radial velocities from dual-channel ATI raw (range uncompressed) SAR data. Data processing scheme is also applied to a RADARSAT-2 acquisition over a section of the Florida Current (FC). Several methods for absolute phase calibration have been attempted and compared. The purpose of attempting several different methods for the absolute phase calibration was to determine the relative performance of these calibration methods, and to assess the potential feasibility of some methods over open ocean (i.e., for scenes that do not contain any land). An approach for coherent averaging (multilooking) based on an analytical model for the homogenous ATI phase is provided. Estimates obtained from SAR ATI measurements are also compared to estimates derived from NASA's OSCAR dataset.

The rest of this article is organized as follows. Section II provides details of the test area and datasets that are used for this study. Section III provides a detailed discussion of the data processing scheme used for the retrieval of surface currents from RADARSAT-2 ATI data. Results obtained after applying the processing scheme on a dataset acquired over a region of the FC are provided and discussed in Section IV. Section V concludes this article.

## II. DATA

Fig. 1 shows a schematic diagram of currents that are present in the vicinity of the chosen study area. The exact area for this study is shown in the figure by the red rectangle. This area covers a portion of the FC that is roughly located between  $80.5\text{--}82^\circ\text{W}$  and  $23\text{--}25.5^\circ\text{N}$ . This location is interesting because here the current typically turns from an easterly (zonal) direction to a northerly (meridional) direction [18]. As shown in Fig. 1, the FC connects the loop current to the GS. Generally, the complex

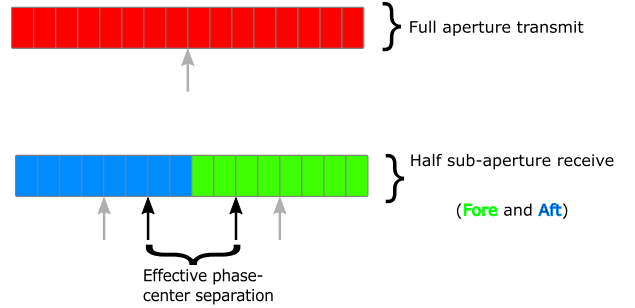


Fig. 2. Antenna configuration of the dual-channel RADARSAT-2 MODEX-1 ATI mode. Gray arrows denote the physical phase centers, and black arrows denote the effective phase centers. Full aperture is used on transmit. Antenna is split into two (fore and aft) on receive. Signal is acquired simultaneously from the two wings that are separated by an effective phase-center separation distance ( $d = 3.75\text{ m}$ ).

dynamics of the FC are driven by processes that operate at a broad range of spatial and temporal scales, including, but not limited to, wind stress, waves, tides, thermohaline density gradient, and hydrological conditions [18]–[21]. However, water mass transport near the surface (i.e., surface currents) are largely driven by wind stress in the Florida Straits [19]–[21].

RADARSAT-2 data over the FC region was acquired using MODEX-1 ScanSAR mode, which is a dual-channel mode for ATI [22]. The antenna configuration for this mode is provided in Fig. 2. The RADARSAT-2 system architecture allows for simultaneous signal acquisition from the two receive channels that are separated in the along-track direction by an effective phase-center separation distance  $d = 3.75\text{ m}$ . Equation (1) provides time-domain expressions for the azimuth received signal from each channel. If the target moves in the radial (slant range) direction during time interval  $\Delta t = \frac{d}{V_s}$ , where  $V_s$  is the satellite velocity, then it will have different range  $R(t)$  in  $z_2(t)$ .

$$\begin{aligned} z_1(t) &= D_1(t) \cdot e^{-j2\pi \frac{R(t)}{\lambda}} \\ z_2(t) &= D_2(t + \Delta t) \cdot e^{-j2\pi \frac{R(t + \Delta t)}{\lambda}} \end{aligned} \quad (1)$$

where  $D(t)$  is the two-way azimuth antenna pattern,  $R(t)$  is slant range, and  $\lambda$  is the radar wavelength. For moving targets, the difference in range between acquisitions  $z_1(t)$  and  $z_2(t)$  can be measured by computing the ATI phase ( $\phi_{\text{ATI}}$ ), as shown in (2). The ATI phase can be converted to the radial velocity ( $V_{\text{rad}}$ ) using the relationship in (3).

$$\phi_{\text{ATI}} = \arg(z_1(t)z_2(t)^*) \quad (2)$$

$$V_{\text{rad}} = \frac{\lambda V_s \phi_{\text{ATI}}}{4\pi d} \quad (3)$$

where  $\arg$  denotes the argument of complex number, and  $*$  indicates complex conjugation. Further details of the RADARSAT-2 dataset are provided in Table I.

As done in [10], estimates derived from SAR ATI are compared to estimates obtained from NASA's Ocean Surface Current Analyses Real-time (OSCAR) dataset, which provides near-surface currents on a spatial grid  $1/3^\circ$  approximately every 5 days [23]–[25]. OSCAR estimates current velocities using sea

TABLE I  
RADARSAT-2 MODEX-1 SCANSAR MODE PARAMETERS

Near Incidence Angle	31.35°
Far Incidence Angle	39.55°
Number of Sub-Beams	2
Nominal Azimuth Resolution	5.7 m
Nominal Slant Range Resolution	8.7 m
Polarization	VV
Orbit Orientation	Descending
Effective Phase Center Separation	3.75 m
Azimuth Oversampling Factor (per sub-beam)	1.37, 1.44
Range Oversampling Factor	1.09
Radar Wavelength	5.55 cm
Acquisition Date & Time (UTC)	2020-07-12 11:18:00

surface height, ocean wind, and sea surface temperature data acquired by satellite *in situ* instruments, and a model based on quasi-linear and steady flow momentum equations. The model estimates a surface current averaged over the top 30 m of the upper ocean. OSCAR provides velocity estimates for zonal and meridional components separately, which are then transformed to radar LOS in this study for comparison with estimates derived from SAR. Accuracy of OSCAR data has been established by comparing velocity observations from buoy drifters deployed at 15 m depth [23]. The standard deviation of difference between OSCAR estimated velocities and observed drifter velocities was found to be 8 and 3 cm/s for zonal and meridional components, respectively [23].

It is important to note that OSCAR cannot be treated as an actual ground truth for RADARSAT-2 dataset. This is because OSCAR provides estimates that have temporal resolution of approximately five days, and estimates from RADARSAT-2 ATI are assumed to be only valid at SAR acquisition time. Velocity estimates obtained from OSCAR are averaged over a surface layer thickness of 30 m [25], whereas estimates obtained from RADARSAT-2 ATI are assumed to be primarily produced by Bragg scattering, which is representative of only a fraction of wavelength from the top surface. Furthermore, there are spatial gaps in OSCAR data near coastal regions. This is because some of the *in situ* data required by OSCAR are not available in coastal regions. Due to these differences, the correlation between surface currents obtained from the two sources is expected to be limited.

Fig. 3 shows the OSCAR estimates obtained after transformation to radar LOS direction and interpolated to a spatial grid obtained from RADARSAT-2 data. The figure clearly shows estimates that can be identified as FC. However, the figure also shows a significant amount of missing data near coastal regions of Cuba and Florida.

### III. DATA PROCESSING

Block diagram of the data processing scheme used for the retrieval of surface radial velocities is shown in Fig. 4. MODEX data are first SAR processed to maximize signal-to-noise ratio (SNR) at each resolution cell. For the ScanSAR dataset, full-aperture SAR processing was performed using the chirp scaling algorithm. Parameters for stationary world were used

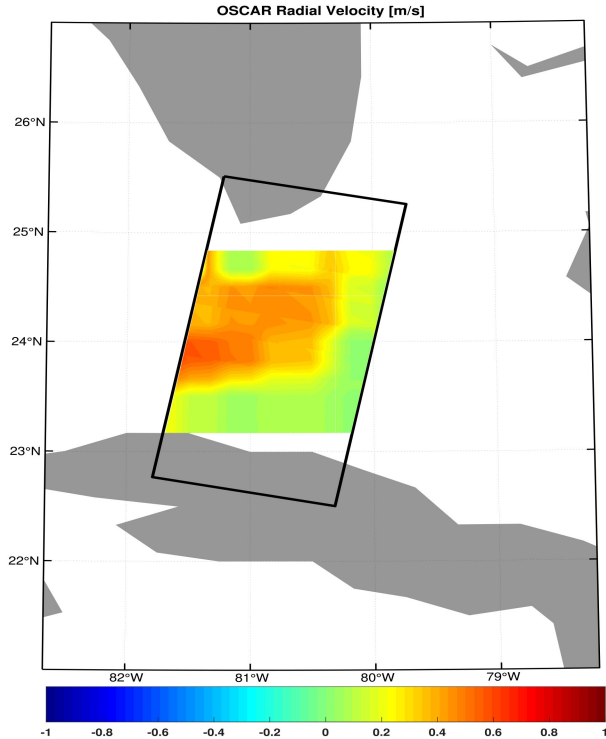


Fig. 3. OSCAR near-surface current transformed to the radar LOS radial velocity estimates and interpolated to a common spatial grid derived from RADARSAT-2 dataset. Black rectangle denotes the swath boundary of RADARSAT-2 acquisition. There is a significant amount of missing data near the coastal regions.

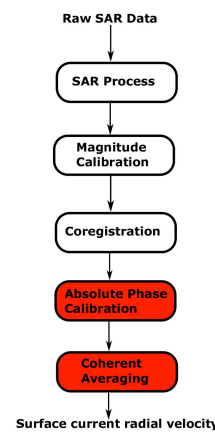


Fig. 4. SAR data processing scheme for the surface current retrieval. Compared to the conventional MTI processing (e.g., for detection/estimation of vessels), blocks highlighted in red are more involved and require special attention.

in the application of chirp scaling and azimuth compression. Full-aperture SAR processing is obtained by padding the interburst gap regions in ScanSAR data with zeros, and then, running the data through a stripmap processor. This preserves the full azimuth resolution of the data, albeit at the cost of some artifacts due to interburst modulations. After SAR processing, coregistration is performed to align ATI samples in space. This can be achieved in time domain by interpolating one channel to a time base that corresponds to the effective phase-center

TABLE II  
RADIAL VELOCITY ESTIMATION ERROR ( $\Delta V_{\text{rad}}$ ) DUE TO ABSOLUTE PHASE CALIBRATION ERROR ( $\Delta\phi_{\text{cal}}$ )

Absolute Phase Calibration Error (radians)	Radial Velocity Estimation Error (cm/s)
0.01	9
0.02	18
0.03	27
0.04	36
0.05	44

separation distance, or by adding a corresponding phase term provided in (4) in the frequency domain.

$$H(f) = e^{j2\pi(f-f_{\text{dc}})\frac{d}{V_s}} \quad (4)$$

where  $f$  is the Doppler frequency, and  $f_{\text{dc}}$  is the Doppler centroid frequency.

After coregistration of ATI samples, the magnitude and phase of the complex multichannel SAR data has to be calibrated. If the scene contains some land, then an adaptive approach for magnitude calibration (e.g., adaptive digital balancing) can be used. Otherwise, the magnitude should be calibrated iteratively by first removing the mean, and then, equalizing the magnitude between channels. This can be achieved by the operations shown in the following equation:

$$\begin{aligned} z_n &= z_n - \langle z_n \rangle \\ z_n &= z_n - \sqrt{\frac{\langle |z_{\text{ref}}|^2 \rangle}{\langle |z_n|^2 \rangle}} \end{aligned} \quad (5)$$

where  $z_n$  is the  $n$ th channel,  $z_{\text{ref}}$  is the reference channel for magnitude equalization,  $\langle \cdot \rangle$  denotes two-dimensional averaging in azimuth and range, and  $|\cdot|$  is the modulus or absolute value.

The final two data processing steps, absolute phase calibration and coherent averaging, are more complicated for surface current retrieval and require particular attention. These are discussed in detail in Sections III-A and III-B.

#### A. Absolute Phase Calibration

For surface currents, radial velocity estimation accuracy is extremely sensitive to errors in the absolute phase calibration. Relationship between radial velocity estimation error ( $\Delta V_{\text{rad}}$ ) and ATI phase calibration error ( $\Delta\phi_{\text{cal}}$ ) is shown in (6). Using this relationship, some values for the radial velocity estimation error were computed and are provided in Table II. For any reliable system with a sufficiently high accuracy, the maximum error in the estimated velocity should be far lower than the expected minimum velocity of the target. Surface currents exhibit radial velocities on the order of a few cm/s on the lower range. If as a heuristic, the maximum tolerable error in the radial velocity estimation is chosen to be 10 cm/s, then Table II shows that the absolute phase calibration error should not exceed  $\sim 0.01$  radians, which is an extremely stringent requirement. Note that in the context of this article, “accuracy” refers to the absolute difference between the estimated radial velocity obtained from ATI measurements and the known or unknown true radial velocity of the target. In literature, this is sometimes referred to as “absolute

accuracy,” as opposed to “relative accuracy,” which refers to the standard deviation of the estimated radial velocity and is related to standard deviation of the measured ATI phase [26], [27]. More discussion on the standard deviation of the measured radial velocity and ATI phase is provided in the context of coherent averaging.

$$\Delta V_{\text{rad}} = \frac{\lambda V_s \Delta\phi_{\text{cal}}}{4\pi d}. \quad (6)$$

For RADARSAT-2 MODEX data, two main sources of the phase error have been identified. These two sources are constant phase error and range-varying phase error. The constant phase error is assumed to be primarily caused by the different characteristics of the two physical receive channels (e.g., circuitry, antenna variations, etc.). The range-varying phase error component is assumed to be primarily caused by the attitude and yaw steering of the antenna. The absolute phase calibration is performed by first correcting for the range-varying phase error, and then, performing the constant phase error correction. The order of operations is important since the range-varying phase error correction can introduce another constant phase offset. Therefore, if the order of operations is reversed, then a second iteration of the constant phase error correction is required.

The range-varying phase error can be removed by first estimating the range-varying component from ATI phase data, and then, appropriately adding the phase to one of the channels. Estimation of this component is performed by coherently averaging in azimuth, and then, applying smoothing to remove any transients. Length of the smoothing filter should be chosen appropriately so that transients from moving targets with a high SNR are filtered out. A polynomial fit can be performed after smoothing to obtain the final estimate of the range-varying phase error component. Let  $\hat{\psi}_{\text{range}}^{p2}$  denote the estimate obtained after performing a second-order polynomial fit of the smoothed estimate. Then, the range-varying phase error can be removed by simply multiplying the estimate with the second channel as follows:

$$\tilde{z}_2 = z_2 \cdot \exp(j\hat{\psi}_{\text{range}}^{p2}) \quad (7)$$

where  $z_2$  is the second channel in time domain, and  $\tilde{z}_2$  denotes the same channel after correction. Note that calibration can also be performed by multiplying the phase function in (7) with the first channel  $z_1$ , however, in this case, conjugate of the phase term should be used. Fig. 5 shows an example of the range-varying phase error, output of the smoothing filter, the second-order polynomial approximation of the smoothed error, and the corrected ATI phase after this error is removed.

The constant phase error correction is performed in a similar manner to range-varying phase error correction (i.e., the error term is estimated from data, and then, removed via a phase multiplication term). In the presence of land in the scene, the constant phase error can be estimated by coherently averaging over all range and azimuth samples that cover land [9], [28], as shown in (8). Another approach that can be applied in the presence of land is adaptive digital balancing, which simultaneously performs magnitude and constant phase calibration by iteratively solving a least-square optimization problem [29]. The adaptive digital

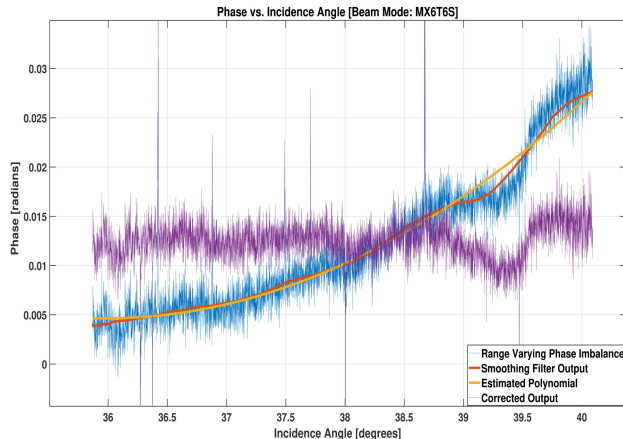


Fig. 5. Example of the range-varying phase error (blue) estimated after averaging the ATI phase in azimuth. Transient spikes are caused by vessels. Red line denotes output of the smoothing filter, and yellow line denotes the polynomial fit. Purple plot shows the output after correcting for the range-varying phase error.

balancing algorithm derived in [29] works only on scenes where land is predominant. An extension of the algorithm that works over maritime scenes with large areas of nonstationary water is provided in Appendix A.

$$\hat{\psi}_{\text{const}}^{\text{land}} = \arg(\langle M_{\text{land}} z_1 z_2^* \rangle) \quad (8)$$

where  $M_{\text{land}}$  is a binary land mask (i.e., valued 1 if the sample is over land, otherwise valued 0), averaging is performed over all samples in range and azimuth.

The constant phase error correction is far more challenging for scenes that do not include any land. For such scenes, two approaches have been introduced in [10] and [30]. In the first approach, the constant phase error is estimated in a similar manner to how it is estimated in the presence of land in (8), except no land mask ( $M_{\text{land}}$ ) is used and the coherent averaging is performed over all samples in the scene [30]. Mathematically, this approach can simply be stated as  $\hat{\psi}_{\text{const}}^{\text{scene}} = \arg(\langle z_1 z_2^* \rangle)$ . This approach assumes that the phase error remains constant in azimuth (slow time) over the area being calibrated. This assumption can be justified for sufficiently long scenes in azimuth that contain high number of stationary scatterers.

In the second approach introduced in [10], the constant phase error is estimated by matching the ATI phase of vessels in the scene to the phase corresponding to their radial velocity obtained from Automatic Identification System (AIS) data. Mathematical derivations for this approach in [10] are only applicable for one vessel per subbeam. A simple extension of this approach is provided in (9), which uses all available vessels per subbeam to estimate the constant phase error. It is simply the average of all the phase differences ( $\phi_n^{\text{AIS}} - \phi_n^{\text{'ATI}}$ ), where  $\phi_n^{\text{AIS}}$  is the phase that corresponds to the radial velocity of the  $n$ th vessel obtained from AIS data, and  $\phi_n^{\text{'ATI}}$  is the uncalibrated ATI phase of the same  $n$ th vessel estimated from the data as shown in (10).

$$\hat{\psi}_{\text{const}}^{\text{vessels}} = \frac{\sum_{n=1}^{N_v} (\phi_n^{\text{AIS}} - \phi_n^{\text{'ATI}})}{N_v} \quad (9)$$

TABLE III  
METHODS FOR CONSTANT PHASE ERROR CORRECTION USED IN THIS STUDY

Method	Description	Requires Stationary Targets (e.g. Land)	Reference
Adaptive Digital Balancing	Calibrate by solving a least squares optimization problem in 2D frequency domain. See Appendix A.	Yes	[8], [29]
Land Calibration	Estimate constant phase error term over land as in Equation 8.	Yes	[9], [28]
Mean Calibration	Estimate constant phase error term by coherently averaging over entire scene.	No	[10], [30]
Vessel Calibration	Estimate constant phase error term using vessels as in Equation 9. Requires vessel AIS data.	No	[10]

where  $N_v$  is total number of vessels used for estimating the constant phase error term  $\hat{\psi}_{\text{vessels}}^{\text{const}}$ . The uncalibrated ATI phase for the  $n$ th vessel estimated from data is

$$\phi_n^{\text{'ATI}} = \arg(\langle M_n^{\text{vessel}} z_1 z_2^* \rangle) \quad (10)$$

where  $M_n^{\text{vessel}}$  denotes the binary mask for  $n$ th vessel. The prime in  $\phi_n^{\text{'ATI}}$  is to denote that this is the uncalibrated ATI phase, as opposed to the calibrated ATI phase. As discussed in [10], this approach is prone to errors due to the limited accuracy of AIS data, and due to the errors associated with interpolation of AIS data to SAR acquisition time. However, it should be noted that the accuracy of this method can potentially be improved with the next generation of space-based SAR systems that will be augmented with on-board AIS sensors. Currently, RADARSAT constellation mission (RCM) has on-board AIS sensors, however, RCM does not have ATI capability.

It should also be noted that the vessel calibration method discussed and applied here is similar to a phase calibration method mentioned in [9] and [28]. However, there is one significant difference between these methods. The phase calibration method mentioned in [9] and [28] suggests using the zero-Doppler position of vessels derived from the intensity image to estimate the radial velocity of vessels, instead of deriving the radial velocity from AIS data, as suggested here. As mentioned in [9] and [28], the true zero-Doppler position is typically difficult to estimate due to the smearing of the moving vessel. For C-band space-based SAR, an even bigger problem with this approach is that in VV polarization, the zero-Doppler position is typically masked by strong returns from the sea clutter, as shown in [31].

Once the constant phase error term is estimated using any of the approaches discussed previously, (7) can be used to calibrate data by appropriately replacing  $\hat{\psi}_{\text{range}}^{\text{P2}}$  with either  $\hat{\psi}_{\text{const}}^{\text{land}}$ ,  $\hat{\psi}_{\text{const}}^{\text{scene}}$ , or  $\hat{\psi}_{\text{const}}^{\text{vessels}}$ . A summary of all available methods for the constant phase error correction is provided in Table III.

### B. Coherent Averaging / Multilooking

Relative to traditional targets of interest for moving target indication (MTI) systems (e.g., vessels and vehicles), scatterers

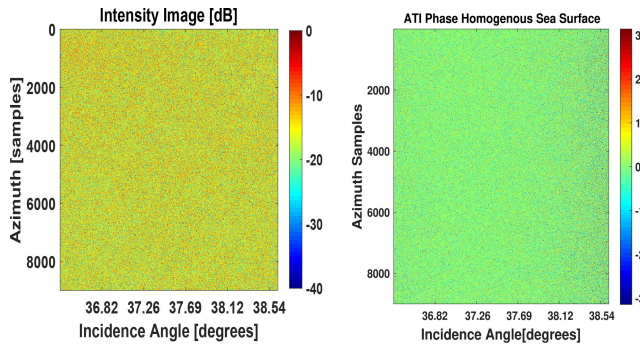


Fig. 6. (Left) Homogenous sea surface intensity and (right) ATI phase image.

from surface currents exhibit very low SNR and radial velocity. However, the scatterers from surface currents are distributed over a large number of resolution cells, and therefore, coherent averaging (multilooking) can be used to improve SNR.<sup>1</sup>

Coherent averaging is typically performed using a 2-D moving average (boxcar) filter [6], [8]. The window size of this filter determines the number of resolution cells or “looks” used for coherent averaging. In literature, it is difficult to find analysis on the impact of different window sizes on ATI phase statistics of real data. In [9], the Cramér–Rao Lower Bound (CRLB) of the interferometric phase is used to describe the affect of coherent averaging on the variance of the ATI phase. However, as noted in [9], the CRLB provides a purely theoretical lower bound on the variance. In practice, the sample variance from real data may not reach this bound. Furthermore, the number of independent looks, which are required for the CRLB expression used in [9] and must be estimated from the data, does not correspond to the number of looks that are actually used for averaging because the looks are not independent in practice. Due to these limitations, a more comprehensive analysis of averaging and its impact on ATI phase statistics of real data is provided here. This analysis provides a practical justification for the window size used for coherent averaging.

Fig. 6 shows single-look intensity and ATI phase images from a patch of the homogenous sea surface (i.e., homogenous intensity and ATI phase). The ATI phase histogram and PDF plots for the single-look case are provided in the yellow and black plots of Fig. 7, respectively. Standard deviations in terms of the ATI phase and radial velocity for this case are also shown in yellow. Radial velocity standard deviation for the single-look case is approximately 6.17 m/s, which is very high when trying to detect surface currents that exhibit velocities on the order of few cm/s to a few m/s [2], [6], [11]. For the single-look case, with such ATI phase statistics, surface currents are indistinguishable from noise. Histogram and PDF plots with coherent averaging/multilooking using a  $4 \times 4$  window are denoted by the blue and red plots in Fig. 7, respectively. Radial velocity standard deviation is approximately 0.96 m/s for this case, which is a significant reduction from the single-look case. The histogram and

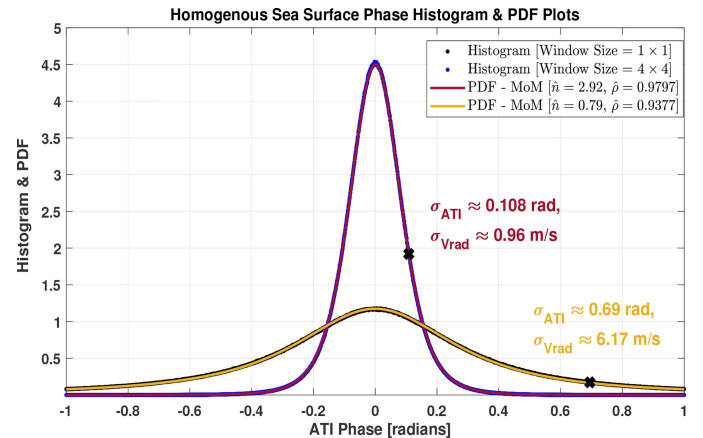


Fig. 7. Histogram/PDF plots with no averaging (black/yellow) and averaging using a  $4 \times 4$  window (blue/red).

PDF plots of Fig. 7 illustrate why coherent averaging is required to improve the detectability of surface currents. Furthermore, as mentioned in Section III-A, the relative accuracy of the ATI phase estimate is also denoted by the standard deviation of the ATI phase estimator. Therefore, coherent averaging is also used to improve the relative accuracy obtained from the ATI phase estimator.

It should be noted that the reduction in the ATI phase standard deviation by coherent averaging comes at a cost of having coarser resolution since the energy from neighboring resolution cells is averaged into one cell. The resulting resolution is dependent on the dimensions of the averaging window in range and azimuth, and the oversampling factor that was used to sample the original data is as follows:

$$\delta_{\text{res}}^{\text{multilook}} = \delta_{\text{res}} \cdot \frac{N_{\text{Win}}}{\Delta_{\text{os}}} \quad (11)$$

where  $\Delta_{\text{os}}$  is the oversampling factor,  $N_{\text{Win}}$  is the window length,  $\delta_{\text{res}}$  is the original resolution, and  $\delta_{\text{res}}^{\text{multilook}}$  is the resulting multilook resolution obtained after coherent averaging.

Since surface currents exhibit radial velocities on the order of a few cm/s at lower end, the standard deviation of the estimated radial velocity should also be on the same order for the reliable detection performance. Fig. 8 shows the histogram and PDF plots for several other window sizes. If a threshold for the standard deviation of the estimated radial velocity is heuristically chosen to be 10 cm/s (0.1 m/s), then Fig. 8 shows that only a window of size  $100 \times 100$  meets this criteria with a standard deviation of 3.55 cm/s. Therefore, for the experimental work presented in this article, a  $100 \times 100$  was chosen since it provides a radial velocity standard deviation that is sufficiently below the heuristically chosen value of 10 cm/s. However, note that from (11) with  $N_{\text{Win}} = 100$ , and parameters from Table I, the resulting slant range resolution degrades to 798 m, and azimuth resolution degrades to 416 and 396 m for the near and far subbeams, respectively.

It was possible to obtain the PDF plots and standard deviations in Figs. 7 and 8, and hence, perform the analysis in this section, because there exists a closed-form expression for the PDF of the

<sup>1</sup>In literature, the term “multilooking” is not used consistently and may also refer to noncoherent averaging. As explicitly stated in the text, here “multilooking” refers to coherent averaging.

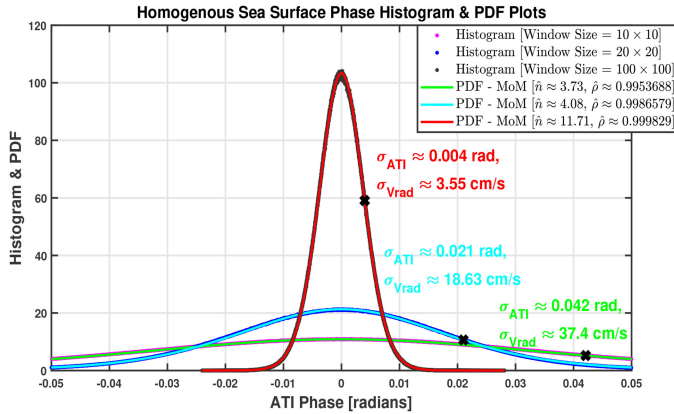


Fig. 8. Histogram/PDF plots with averaging using several different window sizes. Window size of  $100 \times 100$  samples yields a radial velocity standard deviation ( $\sigma_{V_{\text{rad}}}$ ) of  $3.55 \text{ cm/s}$ , which is sufficiently below the heuristically chosen threshold value of  $10 \text{ cm/s}$ .

homogenous ATI phase with integer number of looks  $n$ , which is derived in [32] and stated in (12). For noninteger number of looks, the ATI phase PDF  $f_{\Phi}(\phi)$  can be found by evaluating (12) at closest integers, and then, interpolating to noninteger  $n$ .

$$f_{\Phi}(\phi) = \frac{(1 - \rho^2)^n}{2\sqrt{\pi}\Gamma(n)(1 - \beta^2)^{(n+1/2)}} \left( \sqrt{\pi}\Gamma\left(n + \frac{1}{2}\right)\beta \right. \\ + \frac{\Gamma(n - \frac{1}{2})}{\sqrt{\pi}} \left( \sqrt{1 - \beta^2} + 2(n - \frac{1}{2})\beta \arcsin \beta \right) \\ + \sum_{k=1}^{n-1} \frac{(-1)^k}{2} \frac{\Gamma(k - n + \frac{1}{2})\Gamma(n - k)}{\Gamma(\frac{3}{2} - n)} \\ \left. \times \frac{1 + (2k - 1)\beta^2}{(1 - \beta^2)^{k-n+\frac{1}{2}}} \right) \quad (12)$$

where  $\phi$  is the ATI phase,  $n$  is the number of independent looks (integer),  $\rho$  is magnitude of the complex correlation coefficient, and  $\beta = \rho \cos(\phi - \varphi)$  with  $\varphi$  denoting the mean ATI phase.<sup>2</sup> The standard deviation of the ATI phase ( $\sigma_{\text{ATI}}$ ) is easily obtained by numerical integration of  $f_{\Phi}(\phi)$ . Since the data are oversampled and the resolution cells are not entirely independent,  $n$  does not directly correspond to the number of cells that are used for averaging. For the PDF plots in Figs. 7 and 8, the values of  $n$  and  $\rho$  were estimated using a well-known method called “Method of Moment” [33]. The estimated values,  $\hat{n}$  and  $\hat{\rho}$ , are shown in the legend of Figs 7 and 8.

It should be noted that in general, and especially in the vicinity of surface currents that contain scatterers with varying speeds, the homogenous PDF of (12) does not fit the phase histogram. A heterogeneous mixture model for the PDF, which is simply a superposition of the independent homogenous components present in the scene, provides an ideal fit in such cases [32]. However, since the homogenous components are assumed to

<sup>2</sup>For this analysis, the mean of ATI phase was removed so that the histogram/PDF plots are centered at 0 m/s.

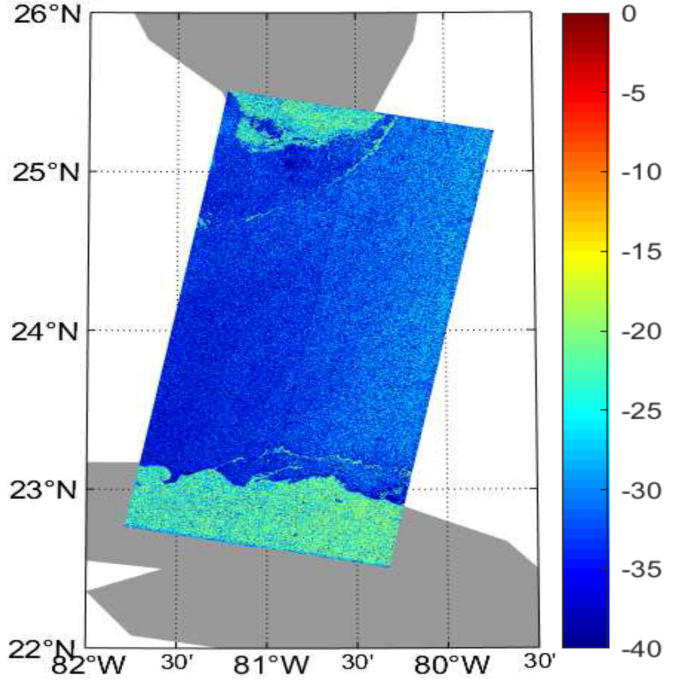


Fig. 9. Single-look intensity image for the scene acquired over the FC.

be independent, the total variance of the heterogeneous mixture model will be the superposition of variances from individual homogenous components that make up the mixture model. So as long as different homogenous components exhibit sufficiently high SNR and coherence similar to what is shown in Figs. 7 and 8, then coherent averaging over heterogeneous scene will provide a similar reduction in variance/standard deviation of the ATI phase. Therefore, in order to determine an approximation for the window size, it is sufficient to examine a homogenous patch of sea surface with exemplary SNR and coherence, as done here.

After coherent averaging, a radial velocity image can be formulated using (3). Another parameter that is important for analysis is the sample coherence for the multilook interferogram, which is provided in (13). The magnitude of sample coherence provides a measure of similarity between ATI samples. Low values of coherence magnitude denote low backscatter from a smooth surface. Hence, the magnitude of sample coherence also provides a measure of confidence in the estimates.

$$\gamma = \frac{\langle z_1 z_2^* \rangle}{\sqrt{\langle z_1 z_1^* \rangle \langle z_2 z_2^* \rangle}}. \quad (13)$$

#### IV. RESULTS AND DISCUSSION

This section provides results obtained after applying the data processing scheme of Section III on RADARSAT-2 MODEX dataset that was acquired over the FC and discussed in Section II. Fig. 9 shows the single-look intensity image. No currents are visible in this image. The magnitude coherence of multilook interferogram is provided in the left image of Fig. 10. The image shows reasonably high values of coherence over water, which

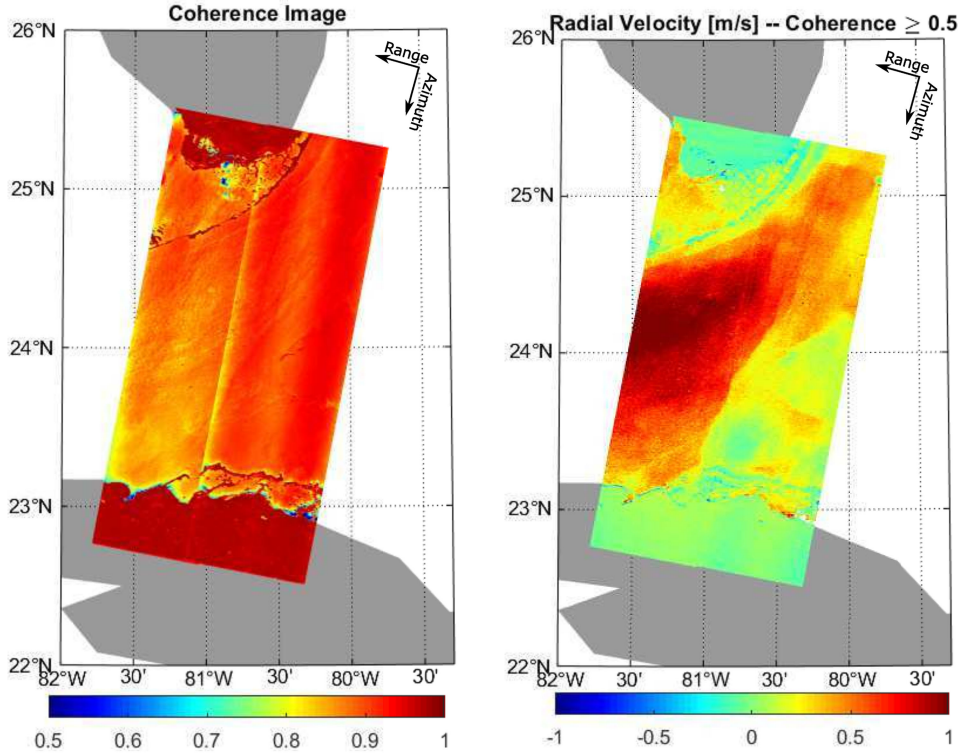


Fig. 10. (Left) Magnitude coherence of the multilook interferogram. (Right) Radial velocity image. Center line in the coherence image that is orientated along the azimuth direction is due to the subbeam boundary. High values of coherence over water indicate a rough sea surface that causes high returns in the backscattered signal. North-westerly moving current in the Florida Strait is clearly visible in the radial velocity image.

is an indication of rough sea surface yielding high returns in the backscattered signal. The line running through the center of the image denotes the subbeam boundary. Since this image was acquired by a right-looking satellite in a descending orbit, the subbeam on the right of the center line is in near range, and the subbeam on the left is in far range. Higher coherence can be observed in the near subbeam, which is expected due to the relatively shallower incidence angles in near range.

The right image in Fig. 10 shows radial velocities computed from the multilook ATI phase. Positive velocities are in the easterly direction, and negative velocities are in westerly direction. The strong current over the expected region is clearly visible in the image. The current is stronger in the far range than the near range, which could potentially be due to the natural weakening, or the fact that the direction of the current is orientated more toward the cross-track/radial direction in the far range. As the current moves more toward the near range (right) in the image, it starts to turn and its orientation becomes more aligned toward along-track, and hence, less sensitive to ATI-based radial velocity measurements.

The difference image between estimates obtained from OSCAR in Fig. 3 and the estimates obtained from SAR ATI in the right image of Fig. 10 is shown in Fig. 11(left). Differences are only shown where OSCAR data are available. As mentioned in Section II, there are gaps in OSCAR due to the unavailability of *in situ* data in coastal regions close to land. Magenta polygon in the difference image denotes the FC boundary that was visually identified in the radial velocity image of Fig. 10, and the black

polygon shows the boundary that was visually identified in the OSCAR image of Fig. 3. In the available data, the two polygons overlap quite well, which shows that currents visually identified from the two sources were spatially aligned.

The difference image shows mostly negative velocities, and since it was computed by subtracting SAR ATI estimates from OSCAR estimates (i.e., OSCAR—SAR ATI), it shows that radial velocity estimates from SAR ATI were consistently higher than radial velocity estimates obtained from OSCAR. This difference can be attributed to several factors. First, the radial velocity measurements from SAR ATI can contain a wind-dependent wave motion component, as shown in [2], [3], and [9]. Without correction of this component, radial velocity estimates do not fully correspond to the underlying surface current. As mentioned in Section II, OSCAR provides estimates that are averaged over the top 30 m of the surface, whereas ATI measurements are assumed to be primarily produced by Bragg scattering, which is representative of only a fraction of wavelength from the top surface. Finally, the two datasets also have significantly different temporal and spatial resolutions. OSCAR dataset was interpolated to the spatial grid obtained from SAR data. Therefore, some differences can be attributed to this interpolation.

Figs. 9–11 show results after applying the adaptive digital balancing method for the constant phase error correction. Analysis was also performed by trying other approaches for the constant phase error correction that are listed in Table III. Radial velocity image using the vessel calibration method is provided and discussed in Appendix B. Radial velocity images obtained

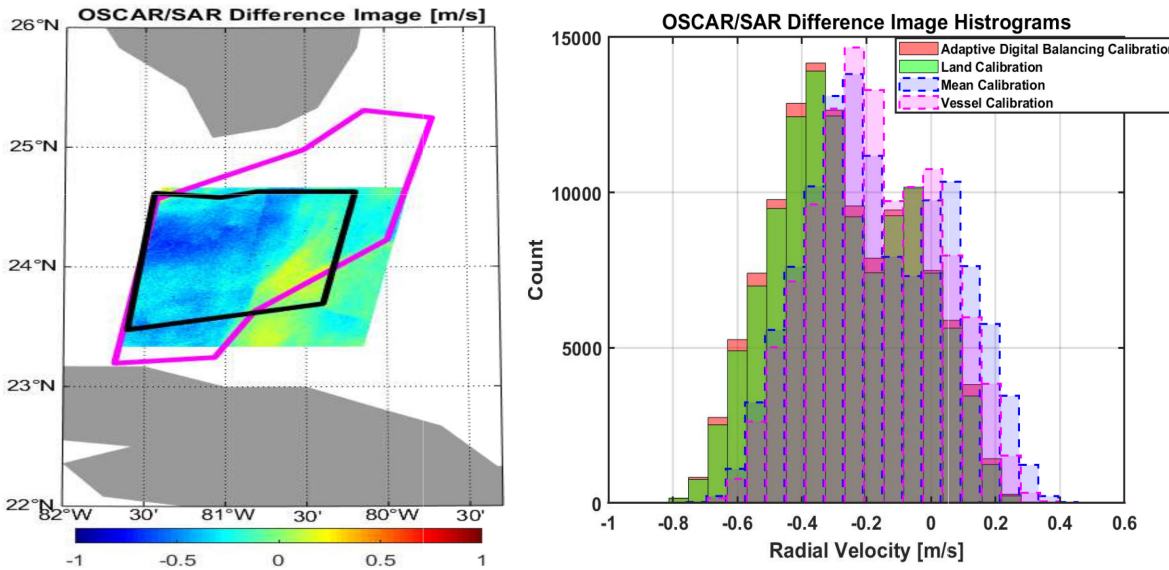


Fig. 11. (Left) Difference image obtained after subtracting RADARSAT-2 ATI radial velocity estimates from OSCAR estimates (i.e., OSCAR—SAR ATI). Magenta polygon denotes the FC boundary identified in the RADARSAT-2 radial velocity image (see Fig. 10), and the black polygon denotes the current boundary identified in the OSCAR radial velocity image (see Fig. 3). (Right) Histogram plots obtained from different calibration approaches over currents identified in SAR ATI (i.e., magenta polygon in the left image).

TABLE IV  
MEAN AND RMS DIFFERENCES BETWEEN OSCAR AND SAR ATI DERIVED  
RADIAL VELOCITY ESTIMATES OBTAINED FROM DIFFERENT  
CALIBRATION METHODS

	Adaptive Digital Balancing	Land	Mean	Vessel
Mean Difference [m/s]	-0.27	-0.27	-0.16	-0.22
RMS Difference [m/s]	0.34	0.34	0.27	0.27

from other calibration methods were visually identical to the radial velocity image in Fig. 10, and are therefore, not repeated. Instead, the histogram plots of OSCAR and SAR ATI differences over currents visually identified in SAR ATI (magenta polygon in difference image of Fig. 11) are provided for each calibration method in the right plot of Fig. 11. Histograms from adaptive digital balancing (red) and land calibration (green) are almost overlapping, which shows that the estimates obtained from these two calibration methods were nearly identical for this particular dataset. Histograms obtained from the mean calibration (blue) and vessel calibration (pink) approaches are slightly offset to the right from adaptive digital balancing and land calibration histograms. The OSCAR/SAR ATI mean and RMS differences observed over currents identified in SAR ATI are provided in Table IV. Overall, the mean and RMS differences obtained from the four calibration methods are approximately within 0.1 m/s of each other. This indicates that different calibration approaches yielded similar results for this particular dataset.

It is important to note that histogram plots in Fig. 11, and the mean and RMS difference values of Table IV, only provide a relative measure of the difference in radial velocity estimates

obtained from the different calibration approaches for this particular dataset. Accordingly, caution is advised on how these should be interpreted. Histogram plots and table values do not provide any absolute measure of performance of one calibration method over another. For example, just because the RMS differences obtained from the mean calibration method are relatively smaller to other calibration methods does not show that this method provides better absolute accuracy. Furthermore, the relative performance of different calibration methods is only valid for this particular dataset. Further studies on more datasets are required to establish the general validity of the positive results obtained from this dataset.

## V. CONCLUSION AND OUTLOOK

This article shows the capability to detect and estimate surface radial velocities with RADARSAT-2 (C-band) dual-channel ATI ScanSAR mode. A detailed presentation of the data processing scheme for surface current retrieval has been provided. Several methods for the constant phase error correction have been attempted. Estimates obtained from these methods were close, with mean and RMS differences within 0.1 m/s. This result shows the potential feasibility of some approaches for open ocean scenes that do not contain any land. However, further studies are required to establish the general validity of these results.

An approach for obtaining the window size for coherent averaging from the analytical expression of the homogenous ATI phase PDF model, and based on requirements for relative accuracy and resolution, has also been presented. This approach is more practical since it provides the sample statistics of real data, unlike the purely theoretical approach that uses CRLB.

Results obtained from SAR ATI over a region of the FC were compared to estimates derived from OSCAR dataset. Qualitative comparison showed high spatial overlap between the currents identified from the two sources. An approximate RMS difference of 0.30 m/s was observed between the two estimates.

SAR ATI estimates derived in this work were not corrected for the bias caused by wind-dependent wave contributions [2], [8], [9]. Future work includes the correction of this bias from external wind data and wind fields derived from SAR data [9], [34], [35]. Further data analysis needs to be performed to validate the positive results obtained in this study. Finally, the study of ocean dynamics is complex and there are many important processes associated with surface currents, including, but not limited to, waves, tides, hydrological conditions, internal waves, etc. [20]. Future work would also focus on the discrimination, detection, and estimation of these important processes associated with surface currents.

#### APPENDIX A

##### ADAPTIVE DIGITAL BALANCING FOR MARITIME SCENES

The adaptive digital balancing algorithm provided in [29] is not well suited for maritime scenes that contain large regions of nonstationary scatters over water. A simple extension is provided here that works well over maritime scenes by utilizing a binary mask that can filter out nonstationary scatterers. The mask could be a land mask (i.e., mask that is 1 when a sample is over land, and 0 otherwise), or it could be a mask that covers man-made structures (e.g., offshore oil rigs).

The extended version of the algorithm works as follows. Given the 2-D Fourier domain signals from each channel  $Z_1(\omega, \Omega)$  and  $Z_2(\omega, \Omega)$ , and a binary mask representing stationary scatterers  $M_{\text{stat}}$ , the goal is to find a set of range frequency and Doppler domain filters  $H_R(\Omega)$  and  $H_D(\omega)$  that minimize the least-squares (LS) error  $e_{\text{LS}}(\omega, \Omega)$  summed over both frequencies.

$$e_{\text{LS}}(\omega, \Omega) = \sum_{\omega} \sum_{\Omega} \left| M_{\text{stat}} \cdot \left( Z_1(\omega, \Omega) - Z_2(\omega, \Omega) H_R(\Omega) H_D(\omega) \right) \right|^2. \quad (14)$$

The LS solution for  $H_R(\Omega)$  and  $H_D(\omega)$  can be found iteratively as

$$\begin{aligned} H_R^{(n+1)}(\Omega) &= \frac{\sum_{\omega} M_{\text{stat}} Z_1(\omega, \Omega) Z_2^{(n)*}(\omega, \Omega)}{\sum_{\omega} |M_{\text{stat}} Z_2^{(n)}(\omega, \Omega)|^2} \\ H_D^{(n+1)}(\omega) &= \frac{\sum_{\Omega} M_{\text{stat}} Z_1(\omega, \Omega) Z_2^{(n)*}(\omega, \Omega)}{\sum_{\Omega} |M_{\text{stat}} Z_2^{(n)}(\omega, \Omega)|^2} \\ Z_2^{(n+1)}(\omega, \Omega) &= Z_2^{(n)}(\omega, \Omega) \cdot \left( H_D^{(n+1)}(\omega) \otimes H_R^{(n+1)\dagger}(\Omega) \right) \end{aligned} \quad (15)$$

where  $\dagger$  denotes conjugate transpose, and  $\otimes$  is the outer product. The iterative process continues until  $|\langle H_R^{(n)}(\Omega) \rangle - \langle H_D^{(n)}(\Omega) \rangle|$  reaches some low threshold (e.g.,  $10^{-4}$ ).

TABLE V  
ESTIMATED RADIAL VELOCITY OF VESSELS AFTER APPLYING ADAPTIVE DIGITAL BALANCING

Vessel ID	AIS Radial Velocity [m/s]	Estimated Radial Velocity [m/s]	Difference [m/s]
001	-2.98	-3.1	0.12
002	2.7	2.86	-0.16
003	3.01	2.99	0.02
004	0.75	0.52	0.23
005	3.03	3.14	-0.11

TABLE VI  
MEAN AND RMS DIFFERENCES AFTER APPLYING VESSEL CALIBRATION METHOD

	Vessel Calibration (All Vessels)	Vessel Calibration (Vessel 004 excluded)
Mean [m/s]	-0.17	-0.22
RMS [m/s]	0.26	0.27

#### APPENDIX B

##### VESSEL CALIBRATION

Radial velocity image obtained after applying the vessel calibration method for absolute phase calibration is shown on the left in Fig. 12. Vessels used for the calibration are also overlaid on the image in bold. For this study, only vessels with AIS contact within 15 min of SAR acquisition time were used for calibration. Further, only large vessels ( $\geq 100$  m) with signatures in the SAR image that were highly correlated with AIS reported vessel positions and sizes were used. Note that only one vessel was used for calibration of the far (left) subbeam.

Comparison of the left image of Fig. 12 with the radial velocity image of Fig. 10 shows similar velocities over the FC, however, higher nonzero velocities, close to 0.2 m/s, are observed over land in the near (right) subbeam of this image, which indicates a miscalibration error. As discussed in Section III-A, the miscalibration error can be attributed to the limited accuracy and interpolation of AIS data. Table V shows the AIS reported and ATI estimated radial velocity of vessels after applying the adaptive digital balancing. Largest difference between the two values is exhibited by Vessel 004. From the table, this difference is approximately 0.2 m/s, which is also close to the amount of shift observed in the near subbeam due to miscalibration. The right image in Fig. 12 was obtained after excluding Vessel 004 for calibration.

Fig. 13 shows histogram plots of OSCAR and SAR radial velocity differences over currents visually identified in SAR ATI (magenta polygon in difference image of Fig. 11) after applying vessel calibration. These plots show slightly higher spread of values after the exclusion of Vessel 004, but the spread is more consistent with other calibration approaches in Fig. 11. Note that the histogram plot for the vessel calibration shown in Fig. 11 was obtained after excluding Vessel 004. The mean and RMS difference values after applying the vessel calibration are provided in Table VI. Comparison of these values with that of Table IV also shows that exclusion of Vessel 004 yields mean and RMS differences that are much closer to estimates obtained from calibration methods applied over land.

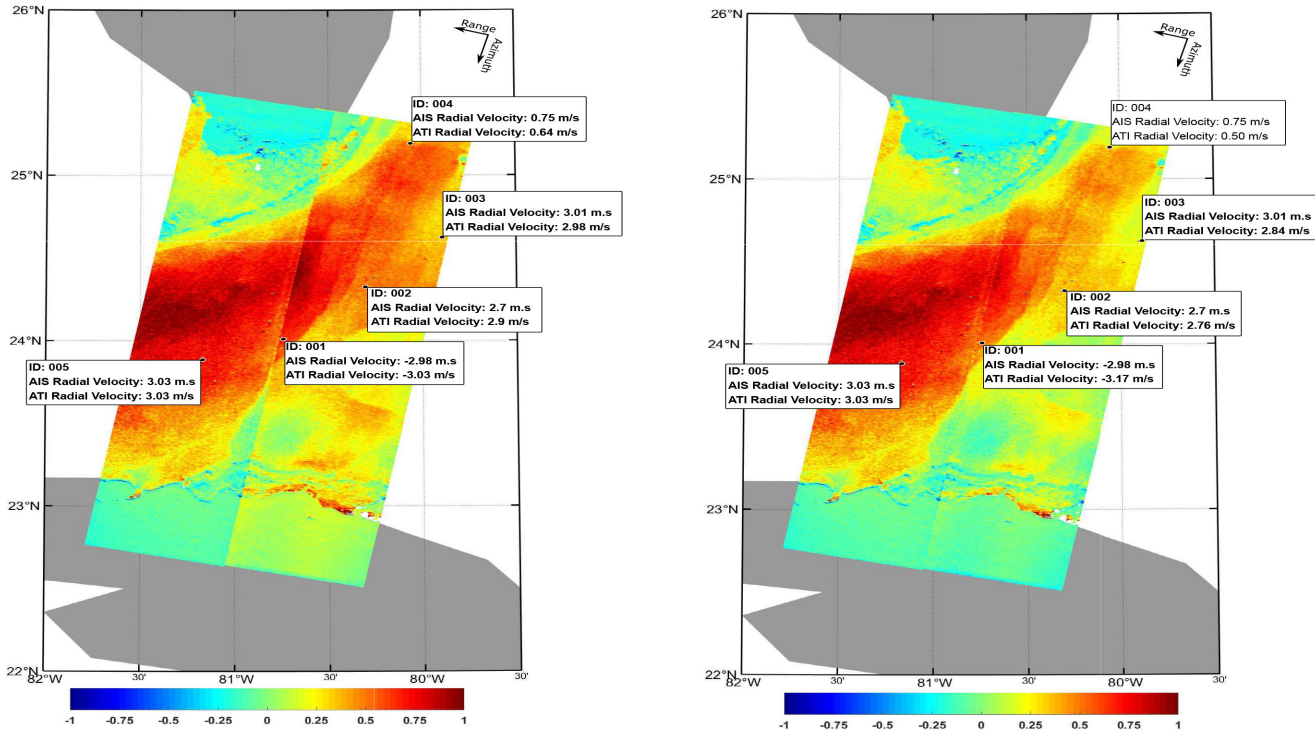


Fig. 12. Radial velocity images obtained after applying the vessel calibration method. Vessels used for calibration are highlighted in bold. Left image was obtained after using all vessels for calibration. The near (right) subbeam in this image is clearly miscalibrated due to the high nonzero values ( $\sim 0.2$  m/s) observed over land. The right image was obtained after excluding Vessel 004 for calibration. Much improved calibration performance over land can be observed in this image.

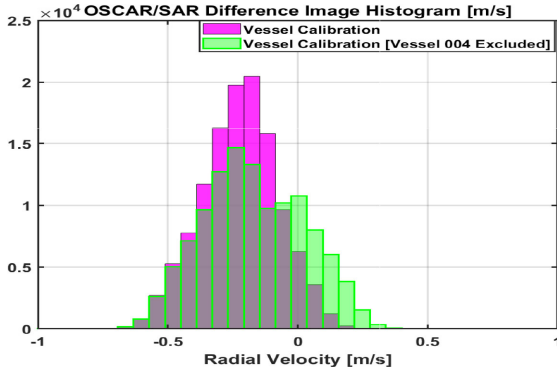


Fig. 13. Histogram plots obtained after vessel calibration.

## REFERENCES

- [1] L. Caesar, S. Rahmstorf, A. Robinson, G. Feulner, and V. Saba, "Observed fingerprint of a weakening Atlantic Ocean overturning circulation," *Nature*, vol. 556, no. 7700, pp. 191–196, 2018.
- [2] D. R. Thompson and J. R. Jensen, "Synthetic aperture radar interferometry applied to ship-generated internal waves in the 1989 Loch Linnhe experiment," *J. Geophys. Res., Oceans*, vol. 98, no. C6, pp. 10 259–10 269, 1993. [Online]. Available: <https://agupubs.onlinelibrary.wiley.com/doi/abs/10.1029/93JC00429>
- [3] R. Romeiser and D. R. Thompson, "Numerical study on the along-track interferometric radar imaging mechanism of oceanic surface currents," *IEEE Trans. Geosci. Remote Sens.*, vol. 38, no. 1, pp. 446–458, Jan. 2000.
- [4] R. Romeiser *et al.*, "Current measurements by SAR along-track interferometry from a Space Shuttle," *IEEE Trans. Geosci. Remote Sens.*, vol. 43, no. 10, pp. 2315–2324, Oct. 2005.
- [5] R. Romeiser, "Surface current measurements by spaceborne along-track InSAR—TerraSAR-X, TanDEM-X, and future systems," in *Proc. IEEE/OES 11th Current Waves Turbulence Meas.*, Mar. 2015, pp. 1–4.
- [6] R. Romeiser, H. Runge, S. Suchandt, R. Kahle, C. Rossi, and P. S. Bell, "Quality assessment of surface current fields from TerraSAR-X and TanDEM-X along-track interferometry and Doppler centroid analysis," *IEEE Trans. Geosci. Remote Sens.*, vol. 52, no. 5, pp. 2759–2772, May 2014.
- [7] R. Romeiser *et al.*, "Current measurements in rivers by spaceborne along-track InSAR," *IEEE Trans. Geosci. Remote Sens.*, vol. 45, no. 12, pp. 4019–4031, Dec. 2007.
- [8] R. Romeiser, S. Suchandt, H. Runge, U. Steinbrecher, and S. Grunler, "First analysis of TerraSAR-X along-track InSAR-derived current fields," *IEEE Trans. Geosci. Remote Sens.*, vol. 48, no. 2, pp. 820–829, Feb. 2010.
- [9] A. Elyouncha, L. E. B. Eriksson, R. Romeiser, and L. M. H. Ulander, "Measurements of sea surface currents in the Baltic Sea region using spaceborne along-track InSAR," *IEEE Trans. Geosci. Remote Sens.*, vol. 57, no. 11, pp. 8584–8599, Nov. 2019.
- [10] M. Rashid and C. Gierull, "Gulf stream detection and estimation with RADARSAT-2 along-track interferometry," in *Proc. IEEE Int. Geosci. Remote Sens. Symp.*, 2020, pp. 1–4.
- [11] K. Biron, W. V. Wychen, and P. W. Vachon, "Gulf stream detection from SAR Doppler anomaly," *Can. J. Remote Sens.*, vol. 44, no. 4, pp. 311–320, 2018.
- [12] W. V. Wychen, P. W. Vachon, J. Wolfe, and K. Biron, "Synergistic RADARSAT-2 and Sentinel-1 SAR images for ocean feature analysis," *Can. J. Remote Sens.*, vol. 45, no. 5, pp. 591–602, 2019. [Online]. Available: <https://doi.org/10.1080/07038992.2019.1662284>
- [13] W. V. Wychen, P. W. Vachon, J. Wolfe, and K. Biron, "The utility of Sentinel-1 data for ocean surface feature analysis in the vicinity of the Gulf Stream," *Can. J. Remote Sens.*, vol. 44, no. 2, pp. 144–152, 2018. [Online]. Available: <https://doi.org/10.1080/07038992.2018.1461558>
- [14] A. Elyouncha, L. E. B. Eriksson, H. Johnsen, and L. M. H. Ulander, "Using Sentinel-1 ocean data for mapping sea surface currents along the southern Norwegian coast," in *Proc. IEEE Int. Geosci. Remote Sens. Symp.*, 2019, pp. 8058–8061.

- [15] C. Livingstone and P. Beaulne, "Modelling RADARSAT-2 Doppler centroids for marine applications," Defence Research and Development Canada, Ottawa, ON, Canada, Tech. Rep. TM 2012-097, 2012.
- [16] R. Romeiser and H. C. Graber, "Current retrieval from moving wave patterns seen by spaceborne SAR," in *Proc. IEEE/OES 12th Current, Waves Turbulence Meas.*, 2019, pp. 1–3.
- [17] M. Sletten, S. Menk, and J. Toporkov, "Comparison of ocean currents derived from UHF ATI-SAR to dispersive shifts observed in sub-aperture image sequences," in *Proc. 13th Eur. Conf. Synthetic Aperture Radar*, 2021, pp. 98–102.
- [18] M. R. Archer, L. K. Shay, and W. E. Johns, "The surface velocity structure of the Florida current in a jet coordinate frame," *J. Geophys. Res., Oceans*, vol. 122, no. 11, pp. 9189–9208, 2017. [Online]. Available: <https://agupubs.onlinelibrary.wiley.com/doi/abs/10.1002/2017JC013286>
- [19] M. R. Archer, L. K. Shay, B. Jaimes, and J. Martinez-Pedraja, "Observing frontal instabilities of the Florida Current using high frequency radar," in *Coastal Ocean Observing Systems*, Y. H. L. Kerkering and R. H. Weisberg, Eds. Boston, MA, USA: Academic Press, 2015, ch. 11, pp. 179–208. [Online]. Available: <https://www.sciencedirect.com/science/article/pii/B978012802227000110>
- [20] H. A. Dijkstra, *Dynamical Oceanography*. Berlin, Germany: Springer, 2008.
- [21] T. N. Lee and E. Williams, "Wind-forced transport fluctuations of the Florida Current," *J. Phys. Oceanogr.*, vol. 18, pp. 937–946, 1988.
- [22] L.-P. Rousseau, C. Gierull, and J. Chouinard, "First results from an experimental ScanSAR-GMTI mode on RADARSAT-2," *IEEE J. Sel. Topics Appl. Earth Observ. Remote Sens.*, vol. 8, no. 11, pp. 5068–5080, Nov. 2015.
- [23] F. Bonjean and G. S. E. Lagerloef, "Diagnostic model and analysis of the surface currents in the tropical Pacific Ocean," *J. Phys. Oceanogr.*, pp. 2938–2954, 2002.
- [24] Earth and Space Research, *OSCAR Third Degree Resolution Ocean Surface Currents*, Version 1, PO.DAAC, Pasadena, CA, USA, 2009.
- [25] J. Hausman, F. Bonjean, and K. Dohan, *Ocean Surface Current Analysis (OSCAR) Third Degree Resolution User's Handbook*, 2009. [Online]. Available: [https://podaac-tools.jpl.nasa.gov/drive/files/allData/oscar/preview/L4/oscar\\_thir\\_deg/docs/oscarthirdguide.pdf](https://podaac-tools.jpl.nasa.gov/drive/files/allData/oscar/preview/L4/oscar_thir_deg/docs/oscarthirdguide.pdf)
- [26] S. Wollstadt, P. López-Dekker, F. De Zan, and M. Younis, "Design principles and considerations for spaceborne ATI SAR-based observations of ocean surface velocity vectors," *IEEE Trans. Geosci. Remote Sens.*, vol. 55, no. 8, pp. 4500–4519, Aug. 2017.
- [27] A. Ferretti *et al.*, "Part C.InSAR processing: A mathematical approach," in *InSAR Principles: Guidelines for SAR Interferometry Processing and Interpretation*. Noordwijk, The Netherlands: ESA Publications, 2007.
- [28] A. Elyouncha, L. E. B. Eriksson, R. Romeiser, and L. M. H. Ulander, "Phase calibration of TanDEM-X ATI-SAR data for sea surface velocity measurements," in *Proc. IEEE Int. Geosci. Remote Sens. Symp.*, 2017, pp. 922–925.
- [29] C. H. Gierull, "Digital channel balancing of along-track interferometric SAR data," Defence Research and Development Canada (DRDC), Ottawa, ON, Canada, Tech. Rep. TM 2003-024, 2003.
- [30] C. H. Gierull, I. C. Sikaneta, and C. E. Livingstone, "Two-aperture SAR channel calibration and GMTI for marine applications," presented at the 8th Int. Conf. Remote Sens. Marine Coastal Environ., Halifax, NS, Canada, May 2005.
- [31] S. Chiu, C. Gierull, and M. Rashid, "Ship detection, discrimination, and motion estimation via spaceborne polarimetric SAR-GMTI," in *Proc. IEEE Radar Conf.*, 2019, pp. 1–6.
- [32] C. H. Gierull, "Closed-form expressions for InSAR sample statistics and its application to non-Gaussian data," *IEEE Trans. Geosci. Remote Sens.*, vol. 59, no. 5, pp. 3967–3980, May 2021.
- [33] C. H. Gierull and I. C. Sikaneta, "Estimating the effective number of looks in interferometric SAR data," *IEEE Trans. Geosci. Remote Sens.*, vol. 40, no. 8, pp. 1733–1742, Aug. 2002.
- [34] G. K. Carvajal, L. E. B. Eriksson, and L. M. H. Ulander, "Retrieval and quality assessment of wind velocity vectors on the ocean with C-band SAR," *IEEE Trans. Geosci. Remote Sens.*, vol. 52, no. 5, pp. 2519–2537, May 2014.
- [35] W. Koch, "Directional analysis of SAR images aiming at wind direction," *IEEE Trans. Geosci. Remote Sens.*, vol. 42, no. 4, pp. 702–710, Apr. 2004.



**Mamoon Rashid** (Member, IEEE) received the B.A.Sc. degree in electrical engineering from the University of Waterloo, Waterloo, ON, Canada, in 2010, and the M.A.Sc. degree in electrical engineering in 2016 from Carleton University, Ottawa, ON, where he is currently working toward the Ph.D. degree in electrical engineering.

From 2012 to 2016, he was with MDA Systems Ltd., Ottawa, as a Defence Contractor for Defence Research and Development Canada (DRDC), where he developed software for space-based synthetic aperture radar (SAR) interferometry and ground moving target indication. Since 2017, he has been a Defence Scientist with the Radar Sensing and Exploitation Section, DRDC, Ottawa. His research interests include signal processing, system modeling, and applications for SAR.



**Christoph H. Gierull** (Senior Member, IEEE) received the Dr.-Ing. degree in electrical engineering from Ruhr-Universität Bochum, Bochum, Germany, in 1995.

From 1991 to 1994, he was a Scientist with the Research Establishment for Applied Science, Wachtberg, Germany. In 1994, he joined the German Aerospace Center (DLR), Oberpfaffenhofen, Germany, where he led the SAR Simulation Group. As part of a DLR team, he assured the X-band interferometric synthetic aperture radar (SAR) performance during the Space-Shuttle Radar Topography Mission with NASA Mission Control, Houston, TX, USA. From 2006 to 2009, he was with Fraunhofer FHR, Wachtberg, Germany. Since 2000, he has been a Senior Defence Scientist with Defence Research and Development Canada, Ottawa, ON, Canada, and in 2010, became the Leader of the Space-Based Radar Group. In 2011, he was appointed as an Adjunct Professor with Université Laval, Quebec City, Canada, and since 2017, also with Simon Fraser University, Burnaby, Canada. He has authored or coauthored numerous journal publications, scientific reports, and a chapter in *Applications of Space-Time Adaptive Processing* (IEE, 2004).

Dr. Gierull is a Co-Editor of, and wrote a chapter in, *Novel Radar Techniques and Applications* (IET, 2017). He filed several Report-of-Inventions and was granted a CAN/US patent on vessel detection in SAR imagery. He was the recipient of the Best Annual Paper Award of the Association of German Electrical Engineers in 1998, a corecipient of the best paper awards at the International Radar Conference 2004, the EUSAR 2006, as well as EUSAR 2016. He was also the recipient of DRDC's highest S&T Performance Excellence Award twice, in 2013 and again in 2020 in addition to the IEEE Geoscience and Remote Sensing Society 2016 J-STARS Paper Award. He and his team also won the Square Dance Arnold Award in 2021. He has been a Technical Advisor to the Canadian Space Agency on several SAR missions including RADARSAT-2, RCM, and its follow-on. In 2021, the European Space Agency selected him as a Member on its Sentinel-1 Next-Generation Mission Advisory Group. He was elected as a Fellow of the IET. He initiated and co-organized the first Special Issue on Multi-Channel Space-Based SAR in the IEEE JOURNAL OF SELECTED TOPICS IN APPLIED EARTH OBSERVATIONS AND REMOTE SENSING in 2015. He was the Associate Editor (AE) for EURASIP's *Signal Processing* in 2004, and since 2019, has been serving as the AE for the IEEE TRANSACTIONS ON GEOSCIENCE AND REMOTE SENSING.